PI(3,5)P_2 asymmetry during mitosis is essential for asymmetric vacuolar inheritance

Mariam Huda[1], Mukadder Koyuncu[1], Cansu Dilege[1], Ayse Koca Caydasi[1]*

[1]Department of Molecular Biology and Genetics, Koç University, Istanbul, Turkey

*Correspondence to: aykoca@ku.edu.tr

Abstract

Phosphatidylinositol 3,5-bisphosphate (PI(3,5)P_2) is a low-abundance signaling lipid that plays crucial roles in various cellular processes, including endolysosomal system structure/function, stress response, and cell cycle regulation. PI(3,5)P_2 synthesis increases in response to environmental stimuli, yet its behavior in cycling cells under basal conditions remained elusive. Here, we analyzed spatiotemporal changes in PI(3,5)P_2 levels during the cell cycle of *S. cerevisiae.* We found that PI(3,5)P_2 accumulates on the vacuole in the daughter-cell while it disappears from the vacuole in the mother-cell during mitosis. Concomitant with the changes in PI(3,5)P_2 distribution, the daughter-vacuole became more acidic, whereas the acidity of the mother-vacuole decreased during mitosis. Our data further showed that both PI(3,5)P_2 and the PI(3,5)P_2 effector protein Atg18 are determinants of vacuolar-pH asymmetry and acidity. Our work, thus, identifies PI(3,5)P_2 as a key factor for establishment of vacuolar-pH asymmetry, providing insights into how the mother cell ages while the daughter cell is rejuvenated.

Running Title

PI(3,5)P_2 is asymmetric during mitosis

Keywords

Asymmetric cell division/Aging/Atg18/Phosphatidylinositol 3,5-bisphosphate/Vacuole

Introduction

Phosphorylated phosphatidylinositol lipids (PIPs) are signaling lipids that serve as master regulators of multiple cellular processes. Phosphatidylinositol-3,5-bisphosphate (PI(3,5)P_2) constitutes one of the least abundant and least understood PIPs. Being a PIP of the endolysosomal system, PI(3,5)P_2 plays critical roles in diverse aspects of cell biology such as membrane trafficking, stress response, vacuole/lysosome structure/function and cell cycle regulation (Han and Emr, 2011; Huda et al., 2023; Jin et al., 2014; Jin and Weisman, 2015; McCartney et al., 2014a; McCartney et al., 2014b; Rutherford et al., 2006).

35

36 PI(3,5)P_2 is synthesized through phosphorylation of the phosphatidylinositol 3-phosphate
37 (PI3P) by the PI3P-5kinase, PIKfyve in humans and Fab1 in yeast (Gary et al., 1998; Sbrissa
38 et al., 1999). In human cells PIKfyve localizes at endolysosomal membranes (early, late,
39 recycling endosomes and lysosomes), predominantly on recycling endosomes (Giridharan et
40 al., 2022). In yeast, Fab1 predominantly decorates the membrane of the vacuole (yeast
41 lysosomes) and localizes to some extend on signaling endosomes (Chen et al., 2021). On
42 these membranes, PIKfyve/Fab1 resides within a protein complex composed of conserved
43 proteins namely Vac14 (ArPIKfyve in humans) and Fig4 (Sac3 in humans) required for
44 PIKfyve/Fab1 function (Barlow-Busch et al., 2023; Dove et al., 2002; Duex et al., 2006a;
45 Lees et al., 2020). In yeast, additionally, a vacuolar membrane protein named Vac7 is part of
46 the Fab1-complex and has an essential role in PI(3,5)P_2 synthesis (Duex et al., 2006a; Duex
47 et al., 2006b).
48

49 Under basal conditions, PI(3,5)P_2 levels are scarce; however, PI(3,5)P_2 abundance increases
50 suddenly in response to environmental stimuli such as insulin treatment in mammalian cells
51 and hyperosmotic shock in budding yeast (Bridges et al., 2012; Duex et al., 2006a; Jones et
52 al., 1999; McCartney et al., 2014b; Sbrissa et al., 1999; Sbrissa and Shisheva, 2005; Tsujita et
53 al., 2004). This is best observed in budding yeast, in which PI(3,5)P_2 levels rise rapidly and
54 transiently up to 20-fold upon hyperosmotic shock (Dove et al., 1997; Duex et al., 2006a).
55 The abrupt response of PI(3,5)P_2 synthesis to hyperosmotic shock made the budding yeast a
56 great model to understand PI(3,5)P_2 regulation and function under hypertonic conditions. A
57 growing body of evidence, however, suggests that PI(3,5)P_2 also functions in cycling cells
58 under basal conditions (Huda et al., 2023; Jin et al., 2014; Jin et al., 2022; Jin and Weisman,
59 2015). Nevertheless, low levels of PI(3,5)P_2 and lack of a well-established biosensor for in
60 vivo detection of PI(3,5)P_2 have been obstacles to the study of PI(3,5)P_2 under isotonic
61 conditions. In yeast, vacuolar localization of the PI(3,5)P_2 binding protein Atg18, which is
62 similar to WIPI proteins in mammals, was shown to correlate well with Fab1 activity (Dove
63 et al., 2004; Efe et al., 2007; Gopaldass et al., 2017). Yet, Atg18 also binds to PI3P (Busse et
64 al., 2015), and the Atg18 mutant that only binds PI(3,5)P_2 but not to PI3P (Atg18-Sloop) has
65 also reduced binding to PI(3,5)P_2 (Gopaldass et al., 2017), challenging its use as an in vivo
66 sensor. Recently, a new probe, SnxA from *Dictyostelium discoideum* was identified as an
67 extremely selective PI(3,5)P_2-binding protein (Vines et al., 2023). Its use as a PI(3,5)P_2

68 reporter was characterized in mammalian cells and in *D. discoideum* (Vines et al., 2023),
69 which now provided the means to study PI(3,5)P_2 under basal conditions.
70
71 In this study, using SnxA and Atg18 as in vivo probes for PI(3,5)P_2, we found that PI(3,5)P_2
72 is asymmetrically present on yeast vacuoles during mitosis. PI(3,5)P_2 accumulated on the
73 membrane of the vacuole that resided in the daughter cell, while it disappeared from the
74 vacuole that stayed in the mother cell. Asymmetry of PI(3,5)P_2 was established shortly before
75 anaphase onset, maintained during anaphase, and diminished with mitotic exit. PI(3,5)P_2
76 precursor PI3P and Fab1-complex components were symmetrically present on the mother and
77 daughter vacuoles, whereas expression of a hyperactive *FAB1* allele caused symmetric
78 distribution of PI(3,5)P_2 suggesting that asymmetric PI(3,5)P_2 production is controlled at the
79 level of Fab1 activity rather than the levels of the precursor or Fab1-complex proteins.
80 Employing a ratiometric in vivo vacuolar-pH sensor, we observed a pH drop in the daughter
81 vacuole, while it increased in the mother vacuole, concomitant with changes in
82 PI(3,5)P_2 distribution during mitosis. We further showed that the asymmetry of PI(3,5)P_2 and
83 the PI(3,5)P_2 effector Atg18 determine the asymmetry of vacuolar pH.
84
85 **Results and Discussion**
86
87 **Yeast codon optimized SnxA can be used as an in vivo sensor for PI(3,5)P_2 in budding**
88 **yeast**
89 In order to monitor PI(3,5)P_2 in budding yeast, we made use of the recently identified
90 genetically coded PI(3,5)P_2 sensor SnxA, which was tested in mammalian cells and in
91 amoebae (Vines et al., 2023). To address whether SnxA would work as an in vivo PI(3,5)P_2
92 sensor in budding yeast, first, we constructed yeast codon-optimized SnxA C-terminally
93 fused with GFP and expressed under TEF1 promoter. Expression of SnxA-GFP integrated
94 into the yeast genome did not alter the vacuole size or cell growth, indicating that SnxA
95 expression does not interfere with PI(3,5)P_2 function (Figure S1A-C). SnxA-GFP colocalized
96 with the vacuolar membrane marker Vph1-3xmCherry in wildtype yeast cells, assessed by
97 Pearson Correlation Coefficient (PCC) (Figure 1A) (Stauffer et al., 2018). Colocalization was
98 lost in the absence of the PI 5-kinase *FAB1*, *VAC7* or *VAC14*, which are essential for
99 PI(3,5)P_2 synthesis (Figure 1A). Thus, we conclude that SnxA vacuole membrane
100 localization is PI(3,5)P_2 dependent in budding yeast. In line with this notion, SnxA co-
101 localization with Vph1 increased in cells expressing a hyperactive Fab1 allele (*fab1-ha, fab1-*

102 *14)* (Duex et al., 2006b), which leads to overproduction of PI(3,5)P_2 (Figure 1B). Likewise,
103 *fab-ha* expression fully rescued the loss of SnxA vacuole localization in *vac14*Δ cells and
104 markedly increased SnxA colocalization with Vph1 in *vac7*Δ cells (Figure 1B), which is
105 consistent with *fab-ha* rescue of PI(3,5)P_2 levels in these cells (Duex et al., 2006b; Gary et
106 al., 2002).
107
108 It is well established by biochemical methods that the amount of PI(3,5)P_2 increases
109 drastically but transiently in response to hyperosmotic shock in budding yeast (Dove et al.,
110 1997; Duex et al., 2006a) – such that within 5 minutes after hyperosmotic shock (0.9M NaCl
111 treatment) PI(3,5)P_2 levels increase ~20 fold, elevated PI(3,5)P_2 persists for ~10 min, after
112 which it starts decreasing, and restores near basal levels ~30 minutes after initial exposure to
113 hyperosmotic shock (Duex et al., 2006a). Hence, to capture the condition with high PI(3,5)P_2
114 levels, we measured SnxA-GFP vacuole periphery localization ~10 min after 0.9M NaCl
115 treatment. SnxA colocalization with Vph1 increased dramatically upon hyperosmotic shock
116 of logarithmically growing wildtype cells (Figure 1C). Salt treatment also caused an increase
117 in SnxA-GFP vacuole periphery localization in *vac14*Δ cells but not in *vac7*Δ and *fab1*Δ
118 (Figure1C), which aligns with previous data that hyperosmotic shock triggers PI(3,5)P_2
119 production in *vac14*Δ cells, albeit at a low level, but not in *vac7*Δ and *fab1*Δ cells (Duex et
120 al., 2006a). We further quantified SnxA vacuole localization upon hyperosmotic shock
121 through time-lapse microscopy. Colocalization of SnxA-GFP with Vph1-3xmCherry
122 prominently increased within the first 2 min following hyperosmotic shock (Figure 1D-E,
123 Supplementary movie 1). High levels of SnxA colocalization with Vph1 were maintained for
124 ~7 min, after which it started decreasing (Figure 1D-E). Colocalization was diminished ~30
125 min after the hyperosmotic shock (Figure 1D-E), in a similar manner measured by
126 biochemical methods (Duex et al., 2006a).
127
128 We further observed that SnxA vacuole localization slightly differed in cells under basal
129 conditions and under hyperosmotic shock as well as in cells expressing *fab1-ha*. While the
130 wildtype cells under basal conditions had SnxA mostly homogenously decorating the vacuole
131 periphery, upon hyperosmotic shock or *fab1-ha* expression SnxA-GFP became concentrated
132 on vacuole-vacuole contact sites and/or fission sites (Contact/Fission, Figure S1D-E) or
133 appeared more concentrated on some parts of the vacuole (patchy appearance, Figure S1D-
134 E), supporting the role of PI(3,5)P_2 in vacuole fission. Notably, under hyperosmotic shock
135 conditions and in cells expressing *fab1-ha* we also noticed that ~20% of the cells had strong

136 SnxA-GFP signal in the vacuolar lumen in addition to the SnxA signal at vacuole periphery
137 (Figure S1E-F), which may indicate additional presence of PI(3,5)P_2 on vacuolar membranes
138 that lacked the Vph1 signal or on other membranes (ie. autophagic vesicles).
139
140 Taken together, these data establish that SnxA can be used as an in vivo sensor for PI(3,5)P_2
141 in budding yeast, similar to its usage in amoeba and mammalian cells (Vines et al., 2023).
142
143 **More PI(3,5)P_2 is present on the daughter vacuole during yeast mitosis**
144 While assessing SnxA-GFP colocalization with Vph1-3xmCherry, we noticed that in cells
145 with segregated vacuoles, SnxA-GFP localization on the vacuole periphery was asymmetric,
146 with a strong preference to localize on the vacuole that resides in the daughter cell
147 compartment (daughter vacuole) (Figure 1A and 1F). On the vacuole of the mother cells
148 (mother vacuole), however, SnxA-GFP was barely detectable (Figure 1A and 1F).
149
150 Next, we asked when SnxA asymmetry was established. To this end, we performed time-
151 lapse microscopy of Vph1-3xmCherry SnxA-GFP containing cells. SnxA-GFP signal was
152 low or undetectable on the vacuole during vacuole segregation to the daughter cell (Figure
153 1G-H). Within 3 minutes after completion of vacuole segregation (t=0), SnxA-GFP
154 accumulated on the daughter vacuole (Figure 1I, Supplementary movie 2). SnxA-GFP signal
155 persisted for ~21 min at the daughter vacuole, after which the signal was greatly reduced
156 (Figure 1J). Quantification of SnxA vacuole periphery localization dynamics revealed that
157 SnxA asymmetry increased for ~15-18 min after vacuole segregation (Figures 1G-H). During
158 this time SnxA localization on the daughter vacuole increased, whereas it was completely
159 diminished from the mother vacuole (Figures 1G-H). After this period, SnxA localization to
160 the daughter vacuole started to decrease, concomitant with a slight increase of SnxA
161 localization on the mother vacuole, causing a decrease in the SnxA asymmetry (Figures 1G-
162 H, Supplementary movie 2). Finally, SnxA localized weakly but equally on both vacuoles,
163 reaching a nearly symmetric state (Figures 1G-H). Using GFP-Tub1 as a mitotic marker, we
164 next addressed the timing of SnxA accumulation on the daughter vacuole with respect to the
165 anaphase onset and mitotic exit. SnxA-3mCherry appeared on the daughter vacuole 3±2 min
166 (mean±SD) before anaphase onset and disappeared near mitotic exit (±5 min) (Figure 1K,
167 Supplementary movie 3).

168 We thus conclude that PI(3,5)P_2 is indeed synthesized in cycling cells under basal conditions.
169 It peaks on the daughter vacuole during mitosis, whereas it disappears from the mother
170 vacuole, creating an asymmetry. PI(3,5)P_2 asymmetry is interrupted with mitotic exit.
171
172 **Atg18 localization at the vacuole periphery correlates with PI(3,5)P_2 levels and mimics**
173 **SnxA localization**
174 As an alternative way to measure PI(3,5)P_2 levels on vacuolar membranes in living cells, we
175 next analyzed the localization of Atg18, a known protein that binds PI(3,5)P_2 with higher
176 affinity, and PI3P with a lower affinity (Dove et al., 2004; Efe et al., 2007; Gopaldass et al.,
177 2017; Takatori et al., 2016). PI(3,5)P_2 binding pool of Atg18 associates with the vacuolar
178 membrane (Gopaldass et al., 2017). In concordance with this, wildtype Atg18-mNeongreen
179 (Atg18-mNG) colocalized with Vph1-3xmCherry in logarithmically growing cells upon
180 hyperosmotic shock (Figure S1G). Atg18-SlooP mutant, which binds PI(3,5)P_2 but not PI3P
181 (Gopaldass et al., 2017), also colocalized with Vph1; whereas the Atg18-FGGG mutant that
182 does not bind PI(3,5)P_2 and PI3P (Gopaldass et al., 2017) failed to localize on the vacuolar
183 membrane (Figure S1G). Atg18-mNG also colocalized with Vph1 under basal conditions
184 (Figure S1H). Hyperosmotic shock or expression of *fab1-ha* increased colocalization of
185 Atg18-mNG with Vph1 (Figure S1H) whereas, deletion of *VAC7* or *VAC14* diminished
186 Atg18 vacuole periphery localization (Figure S1H). Similar to the results obtained using
187 SnxA, *fab1-ha* rescued vacuole localization of Atg18 in both *vac7*Δ and *vac14*Δ cells,
188 whereas salt treatment only rescued vacuole localization in *vac14*Δ (Figure S1H).
189 Accordingly, we conclude that Atg18 localization at the vacuole periphery is indicative of
190 PI(3,5)P_2 levels. Furthermore, time-lapse analysis of Atg18-mNG colocalization with Vph1-
191 3xmCherry yielded similar results to that of SnxA (Figure 2). Atg18 explicitly localized to
192 the vacuole that migrated to the daughter cell, but not to the vacuole that stayed in the mother
193 cell in mitosis (Figure 2A-B, Supplementary movie 4) with similar timing as SnxA (Figure
194 2C-E). Thus, using two independent PI(3,5)P_2 in vivo markers, Atg18 and SnxA, these
195 results establish that PI(3,5)P_2 is specifically present on the daughter vacuole of the yeast
196 during mitosis, whereas it diminishes from the mother vacuole.
197
198 **Levels of PI3P and Fab1-complex components are symmetrically distributed on the**
199 **mother and daughter vacuole**
200 We reasoned that the asymmetry of PI(3,5)P_2 may stem from differential levels of its
201 precursor, PI3P, on mother and daughter vacuoles. To understand whether this is the case, we

202 monitored PI3P in living cells using FYVE domain of mammalian Hrs (Gillooly et al., 2000;
203 Obara et al., 2008). Unlike PI(3,5)P_2, GFP-2xFYVE localized equally on mother and
204 daughter vacuoles (Figure 3A). Thus, PI(3,5)P_2 asymmetry is unlikely to be due to PI3P
205 levels. Alternatively, PI(3,5)P_2 asymmetry may stem from asymmetric distribution of Fab1,
206 Vac7, and Vac14 proteins, which altogether constitute the Fab1-complex. Nevertheless,
207 unlike Atg18, neither of these proteins were asymmetrically distributed on mother and
208 daughter vacuoles (Figure 3B), suggesting that it is the activity of the Fab1 rather than the
209 levels of Fab1-complex proteins on vacuoles that determine the asymmetry of PI(3,5)P_2.
210 Supporting this hypothesis, expression of the hyperactive form of Fab1 (*fab1-ha*) resulted in
211 not only an increment of PI(3,5)P_2 levels but also promoted equal levels of PI(3,5)P_2 on both
212 vacuoles, breaking the PI(3,5)P_2 asymmetry (Figure 3C). Similarly, elevation of Fab1 activity
213 by deletion of *ATG18* (Efe et al., 2007), also disrupted PI(3,5)P_2 asymmetry (Figure 3C).
214 These results altogether support that mechanisms establishing PI(3,5)P_2 asymmetry is likely
215 to regulate Fab1-complex activity, but not the abundance of Fab1-complex proteins on the
216 vacuole periphery or the precursor PI3P.
217
218 **Asymmetry of vacuolar pH is established concomitant with PI(3,5)P_2 asymmetry**
219 Facilitating the assembly and activity of Vph1 containing vacuolar H^+-ATPase (V-ATPase),
220 PI(3,5)P_2 functions in vacuole acidification (Banerjee et al., 2019; Li et al., 2014). Of
221 importance, vacuolar pH also exhibits an asymmetric behavior between mother and daughter
222 cells, such that the daughter vacuole is more acidic than the mother vacuole already before
223 cytokinesis (Henderson et al., 2014; Hughes and Gottschling, 2012). We thus asked whether
224 daughter vacuole acidification coincides with PI(3,5)P_2 accumulation on the daughter
225 vacuole.
226 To assess vacuolar pH we employed the vSEP-mCherry ratiometric pH sensor in which, the
227 vacuole-targeted acid-sensitive fluorophore vSEP is fused with pH-insensitive fluorophore
228 mCherry (Okreglak et al., 2023). Consistent with the previous studies, vacuolar fluorescence
229 intensity of vSEP increased linearly from pH 5 to 8 (Okreglak et al., 2023) (Figure S2A),
230 whereas the mean fluorescence intensity of mCherry remained nearly constant within this pH
231 range (Figure S2B) (Botman et al., 2019). Accordingly, vSEP/mCherry ratios exhibited a
232 linear correlation in the 5-to-8 pH interval (Figure S2C), allowing usage of the
233 vSEP/mCherry ratios in our experiments to evaluate vacuolar pH in this range.
234

235 To address the timing of daughter vacuole acidification, we performed time-lapse microscopy
236 of cells carrying vSEP/mCherry. We quantified vSEP/mCherry ratios in daughter and mother
237 vacuoles separately, and with respect to the timing of vacuole segregation (Figure 4A,
238 Supplementary movie 5). Using our previous data that established dynamic changes of
239 PI(3,5)P_2 as a reference (Figure 1H), we compared the changes in vSEP/mCherry ratio with
240 the changes in PI(3,5)P_2 asymmetry. Our results showed that, shortly after the establishment
241 of PI(3,5)P_2 asymmetry, the pH of the daughter vacuole started to decrease rapidly, while the
242 pH of the mother vacuole started to increase (Figure 4A). This suggests that acidification of
243 the daughter vacuole follows elevation of PI(3,5)P_2 levels on the daughter vacuole, whereas
244 reduction of acidity of the mother vacuole follows the diminishment of PI(3,5)P_2 on the
245 mother vacuole. Supporting this view, concomitant with the reappearance of PI(3,5)P_2 on the
246 mother vacuole (Figure 1H, 18-24 min), the mother vacuole started to regain its acidity
247 (Figure 4A, 18-24 min). Upon establishment of symmetric PI(3,5)P_2, both mother and
248 daughter vacuole pH exhibited similar behavior over time. However, the daughter vacuole
249 remained more acidic than the mother vacuole. Our data thus shows that the vacuolar pH is
250 established soon after vacuole segregation and further indicates that changes in PI(3,5)P_2
251 asymmetry correlate with changes in the vacuolar pH.
252
253 **PI(3,5)P_2 and its asymmetry are crucial for the asymmetry of vacuolar pH**
254 In order to understand whether PI(3,5)P_2 and its asymmetry are required for vacuole acidity
255 and asymmetry of the vacuolar pH, we quantified vSEP/mCherry ratios of daughter and
256 mother vacuoles in the absence of PI(3,5)P_2 (using *vac7*Δ cells) and under conditions that
257 yield symmetric PI(3,5)P_2 distribution (using *fab1-ha* expressing cells). Mother vacuole of
258 wildtype cells had higher vSEP/mCherry ratios than the daughter vacuoles (Figure 4B),
259 consistent with previous reports (Henderson et al., 2014; Hughes and Gottschling, 2012) and
260 our time-lapse data (Figure 4A). Deletion of *VAC7* caused a remarkable increase in the pH of
261 both vacuoles supporting the function of PI(3,5)P_2 in vacuole acidity (Figure 4B).
262 Intriguingly, *VAC7* deletion also resulted in relatively less acidic daughter vacuoles than the
263 mother vacuoles, a situation opposing wildtype cells. *fab1-ha* expression, however, caused
264 more acidic vacuoles and symmetric distribution of pH among the daughter and mother
265 vacuoles in wildtype cells (Figure 4B). Furthermore, *vac7*Δ cells expressing *fab1-ha* had
266 symmetric vacuolar pH, while the overall vacuolar acidity resembled that of the daughter
267 vacuole of the wildtype cells (Figure 5B). These data altogether support that PI(3,5)P_2 is

268 required for vacuole acidification and further suggest that asymmetry of PI(3,5)P_2 is crucial
269 for asymmetry of vacuolar pH.
270
271 **PI(3,5)P_2-mediated vacuole acidification largely depends on Atg18**
272 Next, we analyzed the vacuolar pH in *atg18*Δ cells in which PI(3,5)P_2 appears symmetric on
273 the daughter and mother vacuoles (Figure 3C). However, unexpectedly, we observed that
274 *atg18*Δ cells had overall more alkalinized vacuoles, and similar to *vac7*Δ cells, the
275 asymmetry of vacuolar pH was reversed such that the mother vacuoles were more acidic than
276 the daughter vacuoles (Figure 5A). Analysis of vacuolar pH in *atg18*Δ cells through time-
277 lapse microscopy confirmed the reversed asymmetry of the vacuolar pH (Figure 5B,
278 Supplementary movie 6). Furthermore, vacuolar pH dynamics in the mother appeared more
279 stable during mitosis in *atg18*Δ cells compared to the wildtype cells (Figure 5B), which is in
280 support of a previous report (Okreglak et al., 2023). Thus, Atg18 is critical for vacuole
281 acidity as well as asymmetry and dynamic aspects of vacuolar pH.
282
283 Vacuole acidity of *atg18*Δ cells was fully rescued by the Atg18-Sloop mutant that localizes to
284 the vacuole membrane through binding to PI(3,5)P_2 (Figure 5C). Introduction of the Atg18-
285 FGGG mutant that cannot bind membranes, however, only partially rescued vacuolar pH
286 (Figure 5C), suggesting that Atg18 vacuole periphery localization is necessary for vacuole
287 acidity. Considering that Atg18 vacuole periphery localization requires its binding to
288 PI(3,5)P_2, we propose that Atg18 may have a role downstream of PI(3,5)P_2 in vacuole
289 acidification. We reasoned that if this were the case, artificial recruitment of Atg18 on the
290 membrane of both vacuoles would lead to mother vacuole acidification and symmetric pH. In
291 order to target Atg18 on both mother and daughter vacuoles, we tagged endogenous Vph1
292 and Atg18 at their C-terminus with GFP-binding protein (GBP) and GFP, respectively
293 (Caydasi et al., 2017). This strategy successfully provided symmetric localization of Atg18
294 on the periphery of both vacuoles (Figure 5D). Constitutive presence of Atg18 on both
295 vacuoles did not alter PI(3,5)P_2 asymmetry (Figure 5E), yet caused more acidic and
296 symmetric vacuolar pH (Figure 5F, WT vs Atg18-GFP/GBP). This data supports the role of
297 vacuole membrane localized Atg18 in vacuole acidification. However, PI(3,5)P_2 presence
298 was essential for this role, as constitutive targeting of Atg18 to the vacuolar membranes in
299 *vac7*Δ cells had only a minor effect on vacuole acidity (Figure 5F, *vac7*Δ vs *vac7*Δ Atg18-
300 GFP/GBP). We do not yet know how Atg18 promotes vacuolar acidity. While it may interact
301 with PI(3,5)P_2 to support V-ATPase activity, Atg18 has not been shown to bind V-ATPase

302 subunits. Given its role in transporting vacuolar enzymes (Harding et al., 1996; Yorimitsu
303 and Klionsky, 2005), Atg18's involvement in vacuole acidification may be also related to
304 vacuole biosynthesis and maturation. If this is the case, it likely does not involve Vph1
305 sorting (Finnigan et al., 2012), as Vph1 localization isn't affected by *ATG18* deletion (Figure
306 3C). Atg18's role in vacuole acidification may also be linked to autophagy, which is required
307 for vacuole acidification (Ruckenstuhl et al., 2014). Further research is needed to clarify this
308 connection.
309
310 **PI(3,5)P_2 production on the daughter vacuole is dependent on carbon sources but not on**
311 **Pho85 and amino acid availability**
312 Carbon sources are established regulators of vacuolar pH (Kane, 2016). To address whether
313 they also regulate PI(3,5)P_2 levels, we analyzed SnxA signal upon carbon source withdrawal
314 and in media containing respiratory carbon sources (Ethanol/Glycerol medium). In these
315 media, strikingly, SnxA signal disappeared from both the mother and daughter vacuole
316 peripheries (Figure S2D). This data is in line with the role of PI(3,5)P_2 upstream of V-
317 ATPase assembly (Banerjee et al., 2019; Li et al., 2014) and the disassembly of V-ATPase
318 observed in these media (Kane, 1995; Parra and Kane, 1998). It further suggests that the
319 availability of carbon sources and the respiration/fermentation state of the cell is critical for
320 PI(3,5)P_2 synthesis.
321
322 Next, we tested the contribution of amino acid availability to PI(3,5)P_2 asymmetry in mitotic
323 cells, as availability of some amino acids, such as tyrosine and phenylalanine but not
324 histidine, were shown to influence pH oscillations of the mother vacuole (Okreglak et al.,
325 2023). PI(3,5)P_2 asymmetry was maintained independently of amino acid supplementation
326 (Figure S2E). However, in comparison to the media supplemented with all amino acids,
327 colocalization on the mother vacuole was slightly increased in minimal media supplemented
328 with only histidine, which was rescued by addition of tyrosine or phenylalanine to the media
329 (Figure S2E). This suggests that amino acid availability does not contribute to the increased
330 PI(3,5)P_2 levels on the daughter vacuole during mitosis, but may have a minor impact on the
331 mother vacuole associated PI(3,5)P_2 during mitosis. Analysis of the effect of Pho85 on SnxA
332 asymmetry led to a similar conclusion (Figure S2F). The nutrient responsive cyclin
333 dependent kinase Pho85 phosphorylates Fab1 and is essential for PI(3,5)P_2 production upon
334 hyperosmotic shock (Jin et al., 2014). Pho85 also greatly influences the cell cycle linked pH
335 oscillations of the mother vacuole (Okreglak et al., 2023). When we analyzed SnxA-GFP

336 localization in mitotic cells, we observed that SnxA localization on the mother vacuole was
337 impaired in cells with segregated vacuoles (Figure S2F). This is in line with previous
338 conclusions that the cell cycle dependent oscillation of the mother vacuole is dependent on
339 Pho85 (Okreglak et al., 2023). SnxA daughter vacuole localization, however, did not depend
340 on Pho85 (Figure S2F). Thus, our data suggests presence of a mechanism different than
341 Pho85 dependent phosphorylation of Fab1 to activate the Fab1-complex on the daughter
342 vacuole during mitosis.
343
344 Altogether, our work revealed that the vacuolar signaling lipid PI(3,5)P_2 and its effector
345 protein Atg18 are primarily present on the daughter vacuole during mid-to-late mitosis. Our
346 data further showed that the asymmetry of PI(3,5)P_2 and Atg18 is critical for the asymmetry
347 of vacuolar pH, which is established in mitosis. Notably, a previous study that focused on the
348 pH of mother vacuoles showed that the vacuole alkalinizes before cell division and re-
349 acidifies as cells divide. This oscillation of vacuolar pH was also found to be dependent on
350 PI(3,5)P_2 and Atg18 among other proteins (Okreglak et al., 2023). Our results align with
351 these findings, and further describe how the pH of the daughter vacuole changes during
352 mitosis, as well as how the pH of both vacuoles behaves in relation to the levels of PI(3,5)P_2-
353 Atg18 on the vacuole. Thus, our work establishes a link between PI(3,5)P_2-Atg18 asymmetry
354 and vacuolar pH asymmetry. Given that the decline of vacuolar acidity is a key factor
355 contributing to yeast aging (Henderson et al., 2014; Hughes and Gottschling, 2012), we
356 propose that PI(3,5)P_2 asymmetry, by ensuring that daughter cells have more acidic vacuoles
357 while mother cells have less acidic vacuoles, is one of the mechanisms leading to the aging of
358 the mother cell and the rejuvenation of the daughter cell through asymmetric regulation of
359 vacuolar pH (Figure 5G).
360
361 **Methods**
362
363 **Yeast methods, strains, and plasmids**
364 All yeast strains used in this study are isogenic with S288C and are listed in Table S1. Basic
365 yeast methods and growth media were as described previously (Sherman, 1991). All yeast
366 strains were grown at 30°C, and in synthetic complete media that contained all amino acids
367 and glucose (2%) (SC-media, Glu) (Caydasi and Pereira, 2017) unless otherwise stated. For
368 carbon source withdrawal experiments, cells were brought to log-phase in SC-media and

369 shifted to synthetic media without glucose and with all amino acids (NC) for 2.5 hours before
370 imaging.
371
372 For experiments that analyzed cells in ethanol and glycerol containing media (EG), synthetic
373 media that contained all amino acids but lacked glucose was supplemented with 2% glycerol
374 and 3% ethanol, cells were brought to log-phase in this media. For amino acid depletion or
375 supplementation experiments, MHY333 was brought to log-phase in SC-media, SC-media
376 that lacked all amino acids but histidine (85 mg/l), or in amino acid add back media in which
377 SC-media that lacked all amino acids was supplemented with 85 mg/l of tyrosine or
378 phenylalanine in addition to histidine.
379
380 The cassette PCR-based gene editing method was used for gene deletion and C-terminal
381 tagging of endogenous proteins (Janke et al., 2004; Knop et al., 1999). v-SEP-mCherry
382 containing strains were obtained as described by (Okreglak et al., 2023). GFP-Tubulin,
383 mCherry-Tubulin, SnxA-GFP, SnxA-mCherry, and *fab1-ha* containing yeast were obtained
384 by genome integration of corresponding plasmids. Plasmids used in this study are listed in
385 Table S1.
386
387 SnxA containing plasmids were generated as follows: The SnxA-GFP sequence (Vines et al.,
388 2023) was codon optimized for yeast and synthesized in the pUC18 plasmid under XbaI and
389 SalI restriction sites (pHM001). SnxA-GFP fragment excised by XbaI and SalI was
390 subsequently ligated under TEF1 promoter and CYC1 terminator sequences on p415TEF.
391 The TEF1-SnxA-GFP-CYC fragment was then excised using KpnI and SacI and subcloned
392 into pRS306 to yield pHM007. pHM007 is linearized by ApaI digestion for integration into
393 the *URA3* locus. To construct the SnxA-mCherry containing plasmid, mCherry excised from
394 pAK011 using XhoI and BamHI was used to replace GFP in pHM001. SnxA-mCherry
395 fragment was subcloned under TEF1 promoter and CYC1 terminator sequences on p415TEF
396 using XbaI and SalI. Finally, the TEF1-SnxA-mCherry-CYC fragment was excised using
397 KpnI and SacI and ligated into pRS306 and pRS304 to yield pHM009 and pHM011
398 respectively. pHM009 was digested with ApaI to integrate into *URA3* locus, whereas
399 pHM011 was digested with Kpn2I for integration into *TRP1* locus.
400
401 For integration of Atg18 mutants into the endogenous locus: ~4,3kb Atg18-eGFP-klTRP1
402 fragment amplified from the chromosomal DNA of Atg18-eGFP-klTRP1 containing yeast

403 strain was cloned into pRS315/XmaI&SacII to obtain pCD001. FGGG and Sloop variant
404 containing plasmids (pCD002, pCD003) were obtained through site-directed mutagenesis of
405 pCD001. Atg18-eGFP-klTRP1 fragments of these plasmids were amplified and used as
406 cassettes to replace *atg18*Δ*::hphNT1* in CDY53.
407
408 **Fluorescence Imaging**
409 All microscopy experiments were conducted using a Carl Zeiss Axio Observer 7 motorized
410 inverted epifluorescence microscope, equipped with a Colibri 7 LED light source, Axiocam
411 702 Monochrome camera, 63× Plan Apochromat immersion oil objective lens, Zeiss filter
412 sets 95 (GFP/Cherry) and 44 (FITC), and an XL incubation and climate chamber.
413
414 For time-lapse experiments, cells were grown in filter-sterilized SC-complete media to the
415 log phase and attached to glass-bottom Petri dishes (WVR 10810-054 Matsunami) as
416 previously described (Caydasi and Pereira, 2017). Briefly, the center of the glass dish was
417 coated with 6% Concanavalin A (*Canavalia ensiformis* Jack Bean, type IV Sigma C2010-G)
418 for 10 minutes, then rinsed with sterile water. Next, 200 µL of a logarithmic phase culture
419 was added to the center of the dish and incubated at 30°C for 30 minutes. Non-attached cells
420 were removed by washing with pre-warmed media. The dish was filled with pre-warmed
421 media, placed on the microscope stage, and allowed to sit for 1 hour before starting the
422 experiment. The microscope chamber was preheated to 30°C, 2-3 hours before the
423 experiment. For time-lapse experiments that monitored response to hyperosmotic shock, the
424 glass-bottom petri dish was initially filled halfway with prewarmed media. Once the
425 experiment commenced, 1.8M NaCl dissolved in filter-sterilized SC-Complete media was
426 carefully added at 1:1 ratio (v:v) into the dish on the microscope.
427
428 Time-lapse experiments involving SnxA-GFP without hyperosmotic shock, 3xmCherry-
429 Tubulin, and v-SEP-mCherry *atg18*Δ were conducted with images taken at 3-minute
430 intervals. For Atg18-mNG Vph1-3xmCherry, images were captured at 5-minute intervals.
431 Imaging frequency for GFP-Tubulin, SnxA-GFP with hyperosmotic shock and v-SEP-
432 mCherry WT, the interval was set at 1-minute intervals.
433
434 Still images of cells were captured without cell fixation. Briefly, 1 mL of log-phase culture
435 grown in filter sterilized SC-complete was centrifuged at 3200 rpm for 2 minutes, and cells
436 were resuspended in an appropriate volume of SC-Complete medium before wet mount

437 preparation. A maximum of 3 images were acquired immediately from each slide to prevent
438 stressing of the cells and photobleaching of the signals. For the still images involving
439 hyperosmotic shock, cell suspensions were mixed with 1.8M NaCl containing filter sterilized
440 SC-Complete media at a ratio of 1:1 (v:v) and imaged between 5-10 minutes after salt
441 addition.
442
443 Imaging conditions were as follows: v-SEP-mCherry was imaged using the FITC channel at
444 5% and the mCherry channel at 10%. SnxA-GFP was captured using the FITC channel at
445 10%. Vph1-3xmCherry and 3xmCherry-Tubulin were imaged using the mCherry channel at
446 10%. SnxA-mCherry utilized the mCherry channel at 20%, GFP-Tubulin used the FITC
447 channel at 20%, and Atg18-mNG was imaged using FITC at 15%. 2x2 binning was applied
448 during acquisition. For still images, 13 z-stacks of 0,3 µm thickness were acquired per image.
449 For time-lapse experiments, 9 z-stacks of 0,4 µm thickness were acquired per image.
450
451 **Assessing timing of SnxA and Atg18 vacuole localization**
452 The temporal localization of SnxA and Atg18 on vacuole membranes with respect to vacuole
453 segregation and spindle elongation was judged by eye through monitoring of individual cells
454 from the time-lapse series using Image J (NIH) software.
455
456 For the timing with respect to vacuole segregation, all cells in which segregation of the
457 vacuole can be observed were inspected. Vacuole segregation process usually involves
458 vesicle movement from the mother to daughter at several steps. The end of vacuole
459 segregation was marked as the point after which vesicle movement was not observed.
460 Timepoints at which a clear SnxA or Atg18 fluorescent signal was detected at the mother or
461 daughter vacuole peripheries were noted. The time points of signal appearance and/or
462 disappearance were recorded. Signal persistence was calculated as the duration between
463 signal appearance and disappearance. Timing of signal appearance was calculated as the time
464 between end of vacuole segregation and signal appearance.
465
466 For the timing with respect to spindle elongation, all cells that underwent both the metaphase-
467 to-anaphase transition and the spindle breakdown during the time-lapse duration were
468 analyzed. The timepoints for anaphase onset and spindle breakdown were determined by
469 observing when rapid spindle elongation and spindle breakdown first occurred. The timing of
470 SnxA-GFP and Atg18-mNG signal appearance on the daughter vacuole was calculated with

471 respect to the timing of anaphase onset (t=0). The timing of SnxA-GFP and Atg18-mNG
472 signal disappearance from the daughter vacuole was calculated with respect to the timing of
473 spindle breakdown. To be able to show both timings on the same graph, spindle breakdown
474 timing was normalized to 20 minutes for each cell.
475
476 **Assessing vacuole periphery localization via EzColocalization**
477 To calculate Pearson Correlation Coefficient (PCC) values of Atg18/SnxA/FYVE and Vph1
478 signals, z-projection were performed by summing 4 z-stacks, in which the vacuole was in
479 focus based on the Vph1 reference. Using two reporter inputs and the ROI manager for cell
480 identification, the EzColocalization plugin ImageJ (NIH, Bethesda, Maryland, United States)
481 was used to determine the PCC between Atg18/SnxA/FYVE and Vph1. First, the vacuoles
482 were manually selected from the Vph1 channel using the oval selection tool and added to the
483 ROI manager. In the EzColocalization window, PCC was selected, with the ROI set for cell
484 identification.
485
486 PCC values from time-lapse experiments were obtained in the same way, this time the
487 process was repeated per cell for multiple consequent time points. The time point of end of
488 vacuole segregation (see the section above) was also noted based on Vph1 signal. The PCC
489 values were then aligned according to this timing, mean PCC per timepoint were plotted.
490
491 **Measurement of vacuole diameter**
492 Vacuole diameters were measured in ImageJ, by drawing a line across the vacuole based on
493 the vacuole marker Vph1 on maximum projected images and then using the measure tool.
494
495 **Assessing Protein Asymmetry on Mother and Daughter Vacuoles:**
496 For analysis of protein asymmetry on mother and daughter vacuoles, z-stacks were sum-
497 projected. Daughter to mother ratios of proteins of interest (Figure 4B) were determined
498 using the following equation: $\frac{d[(g_v-g_{bg})/(r_v-r_{bg})]}{m[(g_v-g_{bg})/(r_v-r_{bg})]}$; where m and d represent mother and
499 daughter vacuoles respectively, g denotes mean fluorescence intensity of mNG/GFP (green
500 signal), r means mean fluorescence intensity of mCherry (red signal), v indicates signal on
501 the vacuole, and gb and rb represents the cytosolic signal (background) in the green and red
502 channels respectively. Vacuoles were selected using oval selection tool based on Vph1-
503 3xmCherry signals. Briefly, the same area was used to measure the mean fluorescence

504 intensity of Vph1-3xmCherry and the protein of interest tagged with GFP/mNG. Mean
505 fluorescence intensities were corrected for the background signal by subtracting the
506 cytoplasmic signal from the vacuolar signal. Signal of the protein of interest was normalized
507 by the Vph1-3xmCherry mean fluorescence intensity to obtain the relative levels of protein of
508 interest per unit vacuole membrane (Vph1-3xmCherry serves as a reference). Normalized
509 values of daughter and mother vacuoles were divided to obtain daughter to mother ratios of
510 the protein per unit vacuole membrane.
511
512 **Analysis of vacuolar pH**
513 For analysis of vacuolar pH, z-stacks were sum-projected using ImageJ. Using the oval
514 selection tool, the central region of the vacuole was selected based on mCherry signal. Mean
515 fluorescence intensity of this area was measured in both the v-SEP and mCherry channels.
516 The mean fluorescence intensity of an area free from cells was also measured as the
517 background. Mean fluorescence intensities of v-SEP and mCherry were corrected for
518 background signal by subtracting the background signal from the vacuolar signal.
519 vSEP/mCherry was calculated by dividing the corrected v-SEP signal by the corrected
520 mCherry signal. vSEP/mCherry ratios from time-lapse experiments were obtained in the
521 same way. The time point of end of vacuole segregation was also noted based on mCherry
522 signal. vSEP/mCherry ratios were then aligned according to this time point, vSEP/mCherry
523 ratios per timepoint were plotted.
524
525 **pH sensitivity and calibration curves for vSEP, mCherry and vSEP/mCherry**
526 Cells for pH sensitivity and calibration experiments were prepared as previously described
527 with minor modifications (Okreglak et al., 2023). Briefly, MHY283 strain that has *TEFprom-*
528 *vSEP-mCherry-Cyc1term* integrated into its HO-locus was grown in 10 ml SC-complete
529 medium to log phase. Cells were pelleted at 3200 rpm for 2 min and resuspended in 500 µl
530 dH_2O. 10 µl of cell suspension was pipetted in 90 µl Carmody buffers (Carmody, 1961) at
531 different pH (3-to-10). To this mixture 1 µl of 10% digitonin (in DMSO) was added, mixed
532 and incubated for 20 min at room temperature. Using the cell suspensions, wet mounts were
533 prepared for microscopy. Images were acquired at the brightfield, vSEP and mCherry
534 channels. Signals in the vacuole lumen were quantified as described above (see analysis of
535 vacuolar pH). Corrected vSEP and mCherry mean signal intensities of the vacuole lumen
536 were either plotted individually, or vSEP/mCherry ratios were graphed. Lines (pH 5-to-8
537 range) were fitted with simple linear regression model in Prism.

538

539 **Protein methods**

540 The total yeast cell protein precipitation, sample preparation, and western blotting were
541 performed as previously described (Meitinger et al., 2016). Primary antibodies used were
542 rabbit anti-GFP (Abcam, ab290) and rabbit anti-Tubulin (Abcam, EPR13799). The secondary
543 antibody was goat anti-rabbit HRP-conjugated (Advansta #R-05072-500).
544 Chemiluminescence signals were detected using the Bio-Rad Chemidoc MP system. GFP and
545 tubulin band intensities were measured using ImageJ and corrected for membrane
546 background signal. The area sizes measured were kept constant across all time points.
547 Relative GFP levels were calculated by dividing the background-corrected GFP band
548 intensities by the corresponding background-corrected tubulin band intensities.

549

550 **Spot assay for cell growth comparison on agar plates**

551 Yeast cultures were grown in rich media at 30°C until reaching the stationary phase. The
552 cultures were then adjusted to an OD_{600} of 1, and 10-fold serial dilutions were prepared using
553 sterile 1xPBS. Ten microliters of each serial dilution were spotted onto YPD agar plates and
554 incubated at appropriate temperatures for 1-3 days.

555

556 **Data presentation and Statistical analysis:**

557 Images were visualized and analyzed using ImageJ, figures assembled in Photoshop, and
558 labeled in Illustrator (Adobe, San Jose, CA, USA). Graphs were plotted using Prism 10.2.3
559 (GraphPad, Le Jolla, CA, USA), and statistical significance was determined using one-way
560 ANOVA or unpaired two-tailed t-tests as indicated in the figure legends. In Box-and-whisker
561 plots, boxes extend from the 25th to 75th percentiles, whiskers point to the 10th and 90th
562 percentiles, and lines inside the boxes are the median.

563

564 **Acknowledgements**

565 This study was supported by EMBO installation Grant No. 3918, and TÜBITAK Grant No.
566 219Z100. MH and MK were funded by TÜBITAK Grant No. 122Z887, 219Z100 and
567 118Z979. We would like to thank to Gislene Pereira (University of Heidelberg, Germany),
568 Elmar Schiebel (University of Heidelberg, Germany), Andreas Mayer (University of
569 Lausanne, Switzerland), Keisuke Obara (Nagoya University, Japan), Yoshinori Ohsumi
570 (Tokyo Institute of Technology, Japan), Daniel Gottschling (Calico Life Sciences, USA) and
571 Voytek Okreglak (Altos Labs, USA) for sharing yeast strains and plasmids. We are grateful

572 to Jason King (University of Sheffield, UK) for sharing the sequence of the SnxA reporter
573 prior to its release.

574 **Author Contributions**

575 MH, MK and CD designed and performed the experiments. AKC acquired funding, designed
576 experiments, supervised MH, MK and CD. All authors contributed to the writing of the
577 manuscript.

578 **Conflict of Interest**

579 The authors declare that they have no conflict of interest.
580
581
582

583 **Figure Legends**

584

585 **Figure 1- PI(3,5)P_2 sensor SnxA indicates daughter vacuole specific PI(3,5)P_2 synthesis**
586 **during late mitosis.**

587 A-C. Analysis of SnxA-GFP colocalization with the vacuolar marker Vph1-3xmCherry using
588 still images of log-phase cell populations. Box-and-whisker plots of Pearson Correlation
589 Coefficient (PCC) and representative still images are presented. PCC values were obtained
590 using the EzColocalization plugin in ImageJ by selecting the vacuoles based on Vph1-
591 3xmCherry as a vacuole marker (see materials methods for details). PCC provides a metric
592 for likelihood of co-existence of SnxA-GFP and Vph1-3xmCherry signals in the given area,
593 thus objectively assessing colocalization. Data shown are comparison of wildtype cells (WT)
594 and PI(3,5)P_2 deficient mutants (MHY286, MHY304, MHY302, and AAY007) in (A),
595 comparison of these cells (-) with cells expressing *fab1-ha* (MHY286, MHY288, MHY304,
596 MHY305, MHY302, and MHY303) in (B), and comparison of basal conditions (-) with
597 hyperosmotic shock conditions (+) in (C). Experiments shown in A, B and C were performed
598 altogether, thus the controls (WT, *vac7*Δ, *vac14*Δ and *fab1*Δ) are identical in all graphs. In
599 box-and-whisker plots, boxes extend from the 25th to 75th percentiles. Lines inside the boxes
600 are the median. Whiskers point to the 10th and 90th percentiles. Ordinary one-way ANOVA
601 was performed with Fisher's LSD test. ****: $p<0.0001$, ns: non-significant with $p\geq0.1$. n:
602 sample size. Data shown comes from four independent experiments.

603 D-E. Analysis of the effect of hyperosmotic shock on SnxA-GFP vacuole periphery
604 localization through time-lapse microscopy. Mean PCC values of SnxA-GFP and Vph1-
605 3xmCherry during the time-lapse series are plotted (E) along with images from selected time
606 points of representative cells (D). The graph represents the mean of PCC values obtained
607 from 20 cells (MHY286) subjected to 0.9 M NaCl treatment. Error bars show the standard
608 error of the mean. Red arrows indicate the time point of NaCl addition to the culture dish.
609 Scale bars: 3 μm, BF: bright field.

610 F. Box-and-whisker plots showing PCC values of SnxA-GFP colocalization with the
611 vacuolar marker Vph1-3xmCherry on the mother vacuole (MV) and daughter vacuole (DV)
612 in log-phase WT cells (MHY286) with segregated vacuoles. Boxes show the 25th to 75th
613 percentiles, whiskers point to the 10th and 90th percentiles, and lines inside the boxes are the
614 median. See Figure 1A for representative images. Unpaired two-tailed t-test was performed.
615 ****: $p<0.0001$. Data shown comes from three independent experiments.

616 G-H. Time-lapse microscopy analysis of the SnxA-GFP localization at the vacuole periphery
617 during the cell cycle of WT cells (MHY286). Image series of selected time points from a
618 representative cell is shown in (B). Time-dependent changes in PCC values of SnxA-GFP
619 colocalization with the vacuolar marker Vph1-3xmCherry on the mother and daughter
620 vacuoles are shown in the graph (C). The graph represents the mean of individual cells
621 aligned with respect to the end of vacuole segregation (t=0). Error bars are the standard error
622 of the mean. The white arrow in B indicates the completion of vacuole segregation (t=0). The
623 periods in which PI(3,5)P_2 asymmetry increases (increases), reduces (red.) and disappears are
624 indicated on the graph. Data comes from two independent experiments.
625 I-J. Analysis of SnxA-GFP localization on the mother and daughter vacuole periphery with
626 respect to the timing of SnxA-GFP signal appearance on the daughter vacuole (DV) relative
627 to the end of vacuole segregation (t=0) (I), and the duration of SnxA-GFP localization on the
628 mother vacuole (MV) and daughter vacuole (DV) periphery (J). Circles on scatter plots
629 indicate measurements of individual cells. Black lines in scatter blots are mean and standard
630 deviation. Data comes from two independent experiments.
631 K. Time-lapse microscopy-based analysis of SnxA-mCherry localization with respect to
632 spindle elongation in WT cells containing GFP-Tub1 (MHY295). Selected time points from a
633 representative cell are shown. White arrow marks the time point of anaphase onset (t=0)
634 designated by the start of fast spindle elongation. Yellow arrow marks the timing of spindle
635 breakdown as an indicative of mitotic exit. The graph shows the timing of SnxA-mCherry
636 accumulation on the daughter vacuole (arrival at DV) with respect to the anaphase onset
637 (t=0), and SnxA-mCherry disappearance from the daughter vacuole (departure from DV)
638 with respect to the spindle breakdown (t=20).
639 Scale bars: 3 µm. n: sample size. m: mother, d: daughter
640
641 **Figure 2- Atg18-mNeongreen localizes predominantly to the daughter vacuole**
642 **periphery.**
643 A-D. Time-lapse microscopy-based analysis of Atg18-mNeongreen (Atg18-mNG) vacuole
644 periphery localization during the cell cycle in cells containing Vph1-3xmCherry (MUK089).
645 Selected time points from a representative time-lapse series are shown (A) and mean PCC
646 values of Atg18-mNG colocalization with Vph1-3xmCherry are plotted (B). Data is aligned
647 with respect to the timing of vacuole segregation (t=0) in B and the error bars show the
648 standard deviation. White arrow in A indicates the end of vacuole segregation (t=0). Timing
649 of Atg18-mNG appearance on the daughter vacuole with respect to completion of vacuole

650 segregation (C), and persistence of Atg18-mNG signal on both vacuoles (D) are plotted.
651 Ordinary one-way ANOVA was performed with Fisher's LSD test. **** $p<0.0001$. Data
652 comes from 3 independent timelapse experiments.
653 E. Atg18-mNG daughter vacuole localization with respect to the timing of anaphase onset
654 and spindle breakdown in mCherry-Tub1 containing cells (MUK116). Time-lapse series are
655 of a representative cell are shown. Yellow arrows mark the start of anaphase onset and
656 spindle breakdown respectively. The graph shows Atg18-mNG signal appearance (arrival)
657 and disappearance from the daughter vacuole (departure) relative to the timing of anaphase
658 onset and spindle breakdown, respectively. Data comes from 2 independent timelapse
659 experiments.
660 Scale bars are 3 µm, n: sample size, DV: daughter vacuole, MV: mother vacuole. Circles in
661 scatter plots are values of individual cells. Black lines in scatter plots represent the mean and
662 standard deviation.
663
664 **Figure 3- PI3P and Fab1-complex components localize symmetrically on the vacuole**
665 **periphery.**
666 A. Representative still images and PCC values showing EGFP-2xFYVE colocalization with
667 the vacuolar marker Vph1-3xmCherry in WT cells (MHY252). Unpaired two-tailed t-test
668 was performed. n.s: non-significant with $p=0.9036$. Data shown is from 2 independent
669 experiments.
670 B. Representative still images and daughter vacuole to mother vacuole (DV/MV) ratio of
671 Atg18, Atg18-Sloop, Fab1, Vac14 and Vac7 (MUK089, MUK091, SGY008, SGY009, and
672 MUK117) are shown. The red dashed line marks the DV/MV value of 1, which indicates
673 symmetric distribution on both vacuoles without a preference for a specific vacuole. See
674 materials methods for details.
675 C. Representative still images and PCC values showing SnxA-GFP colocalization with
676 Vph1-3xmCherry on the mother and daughter vacuoles of wildtype (WT) cells and *fab1-ha*
677 or *atg18*Δ mutants (MHY286, MHY288, and MHY289). Data shown is from 2 independent
678 experiments.
679 In the box-and-whisker graphs, boxes show the 25th to 75th percentiles, whiskers show the
680 10th and 90th percentiles; lines inside the boxes are the mean. In B and C, ordinary one-way
681 ANOVA was performed with Fisher's LSD test. ***: $p=0.0002$, **** $p<0.0001$, ns: non-
682 significant with $p\geq0.7441$. Scale bars are 3 µm. BF: bright field.

683

684 **Figure 4- Asymmetry of PI(3,5)P_2 is critical for asymmetry of vacuolar pH.**

685 A. Assessing relative acidity of mother and daughter vacuoles during the cell cycle of
686 wildtype cells (MHY283). v-SEP-to-mCherry ratios (v-SEP/mCherry) of daughter and
687 mother vacuoles serve as an in vivo pH sensor. The graph shows mean v-SEP/mCherry ratios
688 of five cells. Error bars are standard error of the mean. Cells are aligned with respect to the
689 end of vacuole segregation (t=0). Selected time points from the time series of a representative
690 cell are shown. White arrow marks the time of vacuole segregation (t=0). The periods in
691 which PI(3,5)P_2 asymmetry increases (increases), reduces (red.), and disappears are indicated
692 on the graph based on the Figure 2. Data comes from 2 independent experiments. Scale bars:
693 3 μm.

694 B. Representative still images and box-and-whisker plots of v-SEP/mCherry ratios between
695 mother and daughter vacuole in WT (MHY283), *vac7*Δ (MHY291), *fab1-ha* (MHY257), and
696 *vac7*Δ *fab1-ha* (MHY296). Data shown is from 2 independent experiments. Boxes show 25th
697 and 75th percentiles, whiskers indicate 10th and 90th percentiles, the line in the boxes
698 represents the median. Ordinary one-way ANOVA was performed with Fisher's LSD test.
699 **** $p<0.0001$, ** $p=0.0087$, ns: non-significant with $p\geq0.6617$. Scale bar:3 μm, BF: bright
700 field.

701

702 **Figure 5- Vacuole acidity depends on Atg18 and its binding to PI3,5P2.**

703 A. Representative still images and v-SEP/mCherry ratios of mother and daughter vacuoles in
704 WT (MHY283) and *atg18*Δ (MHY277) cells. Data shown is from 2 independent
705 experiments.

706 B. Analysis of vacuolar pH via time-lapse microscopy in *atg18*Δ cells (MHY277). Selected
707 time points from the time series are shown. The graph represents the mean of v-SEP/mCherry
708 ratios of mother and daughter vacuoles as a function of time. Data from individual cells are
709 aligned with respect to the vacuole segregation. Error bars show the standard error of the
710 mean.

711 C. Analysis of vacuolar pH in log-phase culture of WT (MHY283), *atg18*Δ (MHY277),
712 Atg18-Sloop (MHY315), and Atg18-FGGG (MHY317) cells. Data comes from 2
713 independent experiments.

714 D. Atg18-GFP vacuolar localization in cells with and without Vph1-GBP. Representative still
715 images and the percentage of cells in which Atg18-GFP localizes on both vacuoles are shown

716 (MHY223, and SEY082). Graph shows mean of three independent experiments. ~100 cells
717 were counted per strain per experiment. Error bars: standard deviation. ****: $p<0.0001$
718 according to unpaired two-tailed t-test.
719 E. Analysis of SnxA-mCherry vacuole periphery localization in cells carrying Vph1-GFP and
720 Atg18-GFP Vph1-GBP (MHY285, and MHY297).
721 F. Effect of constitutive Atg18 targeting to both vacuoles (Atg18-GFP/GBP) on vacuolar pH
722 (MHY283, MHY297, MHY291, and MHY312). Data shown comes from 2 independent
723 experiments.
724 In box-and-whisker graphs, boxes show the 25th and 75th percentiles, whiskers indicate the
725 10th and 90th percentiles, and the line in the boxes represents the median. In A, C, E and F,
726 ordinary one-way ANOVA was performed with Fisher's LSD test. **** $p<0.0001$, **
727 $p\leq0.0093$, *** $p=0.0004$, and ns: non-significant with $p\geq0.6580$. Scale bars: 3 μm. BF: bright
728 field.
729 G. Working model. $PI(3,5)P_2$ accumulates on the vacuoles of the daughter cell while it is
730 depleted from the vacuoles of the mother cell during mid-to-late mitosis. Concomitantly,
731 daughter cell's vacuole becomes acidified, and acidity of the mother cell's vacuole declines.
732 Thus, presence of $PI(3,5)P_2$ on the daughter vacuole plays a role in daughter cell's
733 rejuvenation and absence of $PI(3,5)P_2$ from the mother vacuole leads to mother cell's aging.
734
735 **Figure S1- Properties of SnxA-GFP and Atg18-mNG as in vivo $PI(3,5)P_2$ sensors**
736 A. SnxA-GFP expression levels in different strains. A representative immunoblot was shown
737 in the bottom. Tub1 was used as a loading control. The graph on the top of each band shows
738 the average of anti-GFP to anti-Tub1 band intensity ratios of from 4 experiments. Error bars:
739 standard error of the mean. Strains used: MHY286, MHY288, MHY293, MHY304,
740 MHY305, MHY303, MHY302, and AAY007.
741 B. Box-and-whisker graph and representative images of vacuole diameters in wildtype (WT),
742 *vac7*Δ and SnxA-GFP containing yeast cells (BBY070, MHY286, and SEY256). Data shown
743 comes from 3 independent experiments. Boxes show 25th and 75th percentiles, whiskers
744 indicate 10th and 90th percentiles, and the line in the boxes represents the median. Ordinary
745 one-way ANOVA was performed with Fisher's LSD test. **** $p<0.0001$, ns: non-significant
746 with $p=0.7079$. Scale bars: 3 μm. BF: bright field.

747 C. Spot assays that show growth of cells with (+SnxA-GFP) or without SnxA-GFP. Serial
748 dilutions of indicated strains (ESM356-1 and MHY286) were spotted on YPD plates and
749 incubated at indicated temperatures.
750 D-F. Vacuolar localization patterns of SnxA.
751 G. Analysis Atg18-mNG colocalization with Vph1-3xmCherry upon hyperosmotic shock.
752 Atg18, Atg8-Sloop mutant, and Atg18-FGGG mutant C-terminally fused with mNeongreen
753 were analyzed (MUK089, MUK090, and MUK091). Atg18-FGGG mutant served as a
754 negative control for vacuole periphery localization. The PCC value of 0.5, indicated with a
755 red dashed line, was selected as a threshold for vacuole membrane localization based on the
756 PCC data of Atg18-FGGG. Data comes from 2 independent experiments.
757 H. Atg18-mNG vacuole localization reflects PI(3,5)P_2 levels. PI(3,5)P_2 levels were
758 manipulated through the use of mutants that are deficient in PI(3,5)P_2 (*vac7*Δ and *vac14*Δ), as
759 well as through the use of *fab1-ha* and 0.9M NaCl treatment in combination with wildtype
760 and *vac7*Δ and *vac14*Δ mutants. PCC values of mNG and Vph1-3xmCherry colocalization
761 were plotted, and representative images were also shown. Analyzed strains: MUK089,
762 MUK098, MUK081, MUK113, MUK080, and MUK110. Data comes from 3 independent
763 experiments.
764 In box-and-whiskers graphs boxes show the 25th and 75th percentiles, whiskers point to the
765 10th and 90th percentile, and the line in the boxes represents the median. In G and H, ordinary
766 one-way ANOVA was performed with Fisher's LSD test. **** $p<0.0001$, and ns: non-
767 significant with $p=0.9908$. Scale bars are 3 μm.
768
769 **Figure S2. pH calibration curves, and the effect of carbon source, amino acids and**
770 **Pho85 on SnxA localization.**
771 A-C. pH sensitivity of vSEP (A), mCherry (B) and pH calibration curve for vSEP/mCherry
772 (C) Pink shaded areas are where vSEP intensity and vSEP/mCherry ratios linearly corralates
773 with pH. Green shaded area in C marks the vSEP/mCherry ratios within the linear range.
774 Data comes from 2 independent experiments. In each experiment, at least 100 vacuoles were
775 quantified per different pH. Error bars are standard deviation. Fitted lines were obtained with
776 simple linear regression model in Prism.
777 D-F. Analysis of SnxA-GFP localization at the vacuole periphery with respect to the carbon
778 source (D), amino acid supplementation (E) and presence of Pho85 (F). Representative still
779 images were shown and PCC values were ploted. Data comes from 3 independent
780 experiments.

781 In box-and-whiskers graphs boxes show the 25th and 75th percentiles, whiskers point to the
782 10th and 90th percentile, and the line in the boxes represents the median. Ordinary one-way
783 ANOVA was performed with Fisher's LSD test. **** $p<0.0001$. Scale bars are 3 μm.
784
785 **Supplementary Table**
786 Table S1. List of strains and plasmids used in the study
787
788 **Description of Supplementary movies**
789 **Supplementary movie 1:** Timelapse movie of SnxA-GFP Vph1-3xmCherry containing yeast
790 strain (MHY286) upon 0.9M NaCl treatment between the first and second timepoints. The
791 channels from left to right are GFP, mCherry, and merge.
792 **Supplementary movie 2:** Timelapse movie of SnxA-GFP Vph1-3xmCherry containing yeast
793 strain (MHY286). The channels from left to right are GFP, mCherry, and merge.
794 **Supplementary movie 3:** Timelapse movie of SnxA-mCherry GFP-Tub1 containing yeast
795 strain (MHY295). The channels from left to right are mCherry, GFP and merge.
796 **Supplementary movie 4:** Timelapse movie of Atg18-mNeongreen containing yeast strain
797 (MUK089). The channels from left to right are mNeongreen, mCherry, and merge.
798 **Supplementary movie 5:** Timelapse movie of vSEP-mCherry containing yeast strain
799 (MHY283). The channels from left to right are vSEP, mCherry, and merge.
800 **Supplementary movie 6:** Timelapse movie of vSEP-mCherry containing *atg18*Δ yeast strain
801 (MHY277). The channels from left to right are vSEP, mCherry, and merge.
802
803
804

805 **References**

806 Banerjee, S., K. Clapp, M. Tarsio, and P.M. Kane. 2019. Interaction of the late endo-
807 lysosomal lipid PI(3,5)P2 with the Vph1 isoform of yeast V-ATPase increases its
808 activity and cellular stress tolerance. *J Biol Chem*. 294:9161-9171.
809 Barlow-Busch, I., A.L. Shaw, and J.E. Burke. 2023. PI4KA and PIKfyve: Essential
810 phosphoinositide signaling enzymes involved in myriad human diseases. *Curr Opin*
811 *Cell Biol*. 83:102207.
812 Botman, D., D.H. de Groot, P. Schmidt, J. Goedhart, and B. Teusink. 2019. In vivo
813 characterisation of fluorescent proteins in budding yeast. *Sci Rep*. 9:2234.
814 Bridges, D., J.T. Ma, S. Park, K. Inoki, L.S. Weisman, and A.R. Saltiel. 2012.
815 Phosphatidylinositol 3,5-bisphosphate plays a role in the activation and subcellular
816 localization of mechanistic target of rapamycin 1. *Mol Biol Cell*. 23:2955-2962.
817 Busse, R.A., A. Scacioc, R. Krick, A. Perez-Lara, M. Thumm, and K. Kuhnel. 2015.
818 Characterization of PROPPIN-Phosphoinositide Binding and Role of Loop 6CD in
819 PROPPIN-Membrane Binding. *Biophys J*. 108:2223-2234.
820 Carmody, W.R. 1961. Easily prepared wide range buffer series. *Journal of Chemical*
821 *Education* 38.
822 Caydasi, A.K., A. Khmelinskii, R. Duenas-Sanchez, B. Kurtulmus, M. Knop, and G. Pereira.
823 2017. Temporal and compartment-specific signals coordinate mitotic exit with spindle
824 position. *Nat Commun*. 8:14129.
825 Caydasi, A.K., and G. Pereira. 2017. Evaluation of the Dynamicity of Mitotic Exit Network
826 and Spindle Position Checkpoint Components on Spindle Pole Bodies by
827 Fluorescence Recovery After Photobleaching (FRAP). *Methods Mol Biol*. 1505:167-
828 182.
829 Chen, Z., P.C. Malia, R. Hatakeyama, R. Nicastro, Z. Hu, M.P. Peli-Gulli, J. Gao, T.
830 Nishimura, E. Eskes, C.J. Stefan, J. Winderickx, J. Dengjel, C. De Virgilio, and C.
831 Ungermann. 2021. TORC1 Determines Fab1 Lipid Kinase Function at Signaling
832 Endosomes and Vacuoles. *Curr Biol*. 31:297-309 e298.
833 Dove, S.K., F.T. Cooke, M.R. Douglas, L.G. Sayers, P.J. Parker, and R.H. Michell. 1997.
834 Osmotic stress activates phosphatidylinositol-3,5-bisphosphate synthesis. *Nature*.
835 390:187-192.
836 Dove, S.K., R.K. McEwen, A. Mayes, D.C. Hughes, J.D. Beggs, and R.H. Michell. 2002.
837 Vac14 controls PtdIns(3,5)P(2) synthesis and Fab1-dependent protein trafficking to
838 the multivesicular body. *Curr Biol*. 12:885-893.
839 Dove, S.K., R.C. Piper, R.K. McEwen, J.W. Yu, M.C. King, D.C. Hughes, J. Thuring, A.B.
840 Holmes, F.T. Cooke, R.H. Michell, P.J. Parker, and M.A. Lemmon. 2004. Svp1p
841 defines a family of phosphatidylinositol 3,5-bisphosphate effectors. *EMBO J*.
842 23:1922-1933.
843 Duex, J.E., J.J. Nau, E.J. Kauffman, and L.S. Weisman. 2006a. Phosphoinositide 5-
844 phosphatase Fig 4p is required for both acute rise and subsequent fall in stress-
845 induced phosphatidylinositol 3,5-bisphosphate levels. *Eukaryotic cell*. 5:723-731.
846 Duex, J.E., F. Tang, and L.S. Weisman. 2006b. The Vac14p-Fig4p complex acts
847 independently of Vac7p and couples PI3,5P2 synthesis and turnover. *J Cell Biol*.
848 172:693-704.
849 Efe, J.A., R.J. Botelho, and S.D. Emr. 2007. Atg18 regulates organelle morphology and Fab1
850 kinase activity independent of its membrane recruitment by phosphatidylinositol 3,5-
851 bisphosphate. *Mol Biol Cell*. 18:4232-4244.
852 Finnigan, G.C., G.E. Cronan, H.J. Park, S. Srinivasan, F.A. Quiocho, and T.H. Stevens. 2012.
853 Sorting of the yeast vacuolar-type, proton-translocating ATPase enzyme complex (V-

854 ATPase): identification of a necessary and sufficient Golgi/endosomal retention signal
855 in Stv1p. *J Biol Chem*. 287:19487-19500.
856 Gary, J.D., T.K. Sato, C.J. Stefan, C.J. Bonangelino, L.S. Weisman, and S.D. Emr. 2002.
857 Regulation of Fab1 phosphatidylinositol 3-phosphate 5-kinase pathway by Vac7
858 protein and Fig4, a polyphosphoinositide phosphatase family member. *Mol Biol Cell*.
859 13:1238-1251.
860 Gary, J.D., A.E. Wurmser, C.J. Bonangelino, L.S. Weisman, and S.D. Emr. 1998. Fab1p is
861 essential for PtdIns(3)P 5-kinase activity and the maintenance of vacuolar size and
862 membrane homeostasis. *J Cell Biol*. 143:65-79.
863 Gillooly, D.J., I.C. Morrow, M. Lindsay, R. Gould, N.J. Bryant, J.M. Gaullier, R.G. Parton,
864 and H. Stenmark. 2000. Localization of phosphatidylinositol 3-phosphate in yeast and
865 mammalian cells. *EMBO J*. 19:4577-4588.
866 Giridharan, S.S.P., G. Luo, P. Rivero-Rios, N. Steinfeld, H. Tronchere, A. Singla, E.
867 Burstein, D.D. Billadeau, M.A. Sutton, and L.S. Weisman. 2022. Lipid kinases
868 VPS34 and PIKfyve coordinate a phosphoinositide cascade to regulate retriever-
869 mediated recycling on endosomes. *Elife*. 11.
870 Gopaldass, N., B. Fauvet, H. Lashuel, A. Roux, and A. Mayer. 2017. Membrane scission
871 driven by the PROPPIN Atg18. *EMBO J*. 36:3274-3291.
872 Han, B.K., and S.D. Emr. 2011. Phosphoinositide [PI(3,5)P2] lipid-dependent regulation of
873 the general transcriptional regulator Tup1. *Genes Dev*. 25:984-995.
874 Harding, T.M., A. Hefner-Gravink, M. Thumm, and D.J. Klionsky. 1996. Genetic and
875 phenotypic overlap between autophagy and the cytoplasm to vacuole protein targeting
876 pathway. *J Biol Chem*. 271:17621-17624.
877 Henderson, K.A., A.L. Hughes, and D.E. Gottschling. 2014. Mother-daughter asymmetry of
878 pH underlies aging and rejuvenation in yeast. *Elife*. 3:e03504.
879 Huda, M., S.N. Bektas, B. Bekdas, and A.K. Caydasi. 2023. The signalling lipid PI3,5P(2) is
880 essential for timely mitotic exit. *Open Biol*. 13:230125.
881 Hughes, A.L., and D.E. Gottschling. 2012. An early age increase in vacuolar pH limits
882 mitochondrial function and lifespan in yeast. *Nature*. 492:261-265.
883 Janke, C., M.M. Magiera, N. Rathfelder, C. Taxis, S. Reber, H. Maekawa, A. Moreno-
884 Borchart, G. Doenges, E. Schwob, E. Schiebel, and M. Knop. 2004. A versatile
885 toolbox for PCR-based tagging of yeast genes: new fluorescent proteins, more
886 markers and promoter substitution cassettes. *Yeast*. 21:947-962.
887 Jin, N., K. Mao, Y. Jin, G. Tevzadze, E.J. Kauffman, S. Park, D. Bridges, R. Loewith, A.R.
888 Saltiel, D.J. Klionsky, and L.S. Weisman. 2014. Roles for PI(3,5)P2 in nutrient
889 sensing through TORC1. *Mol Biol Cell*. 25:1171-1185.
890 Jin, Y., N. Jin, Y. Oikawa, R. Benyair, M. Koizumi, T.E. Wilson, Y. Ohsumi, and L.S.
891 Weisman. 2022. Bur1 functions with TORC1 for vacuole-mediated cell cycle
892 progression. *EMBO Rep*. 23:e53477.
893 Jin, Y., and L.S. Weisman. 2015. The vacuole/lysosome is required for cell-cycle
894 progression. *Elife*. 4.
895 Jones, D.R., A. Gonzalez-Garcia, E. Diez, A.C. Martinez, A.C. Carrera, and I. Merida. 1999.
896 The identification of phosphatidylinositol 3,5-bisphosphate in T-lymphocytes and its
897 regulation by interleukin-2. *J Biol Chem*. 274:18407-18413.
898 Kane, P.M. 1995. Disassembly and reassembly of the yeast vacuolar H(+)-ATPase in vivo. *J*
899 *Biol Chem*. 270:17025-17032.
900 Kane, P.M. 2016. Proton Transport and pH Control in Fungi. *Adv Exp Med Biol*. 892:33-68.
901 Knop, M., K. Siegers, G. Pereira, W. Zachariae, B. Winsor, K. Nasmyth, and E. Schiebel.
902 1999. Epitope tagging of yeast genes using a PCR-based strategy: more tags and
903 improved practical routines. *Yeast*. 15:963-972.

904 Lees, J.A., P. Li, N. Kumar, L.S. Weisman, and K.M. Reinisch. 2020. Insights into
905 Lysosomal PI(3,5)P(2) Homeostasis from a Structural-Biochemical Analysis of the
906 PIKfyve Lipid Kinase Complex. *Mol Cell*. 80:736-743 e734.
907 Li, S.C., T.T. Diakov, T. Xu, M. Tarsio, W. Zhu, S. Couoh-Cardel, L.S. Weisman, and P.M.
908 Kane. 2014. The signaling lipid PI(3,5)P(2) stabilizes V(1)-V(o) sector interactions
909 and activates the V-ATPase. *Mol Biol Cell*. 25:1251-1262.
910 McCartney, A.J., Y. Zhang, and L.S. Weisman. 2014a. Phosphatidylinositol 3,5-
911 bisphosphate: low abundance, high significance. *BioEssays : news and reviews in*
912 *molecular, cellular and developmental biology*. 36:52-64.
913 McCartney, A.J., S.N. Zolov, E.J. Kauffman, Y. Zhang, B.S. Strunk, L.S. Weisman, and
914 M.A. Sutton. 2014b. Activity-dependent PI(3,5)P2 synthesis controls AMPA receptor
915 trafficking during synaptic depression. *Proc Natl Acad Sci U S A*. 111:E4896-4905.
916 Meitinger, F., S. Palani, and G. Pereira. 2016. Detection of Phosphorylation Status of
917 Cytokinetic Components. Springer New York. 219-237.
918 Obara, K., T. Noda, K. Niimi, and Y. Ohsumi. 2008. Transport of phosphatidylinositol 3-
919 phosphate into the vacuole via autophagic membranes in Saccharomyces cerevisiae.
920 *Genes Cells*. 13:537-547.
921 Okreglak, V., R. Ling, M. Ingaramo, N.H. Thayer, A. Millett-Sikking, and D.E. Gottschling.
922 2023. Cell cycle-linked vacuolar pH dynamics regulate amino acid homeostasis and
923 cell growth. *Nat Metab*. 5:1803-1819.
924 Parra, K.J., and P.M. Kane. 1998. Reversible association between the V1 and V0 domains of
925 yeast vacuolar H+-ATPase is an unconventional glucose-induced effect. *Mol Cell*
926 *Biol*. 18:7064-7074.
927 Ruckenstuhl, C., C. Netzberger, I. Entfellner, D. Carmona-Gutierrez, T. Kickenweiz, S.
928 Stekovic, C. Gleixner, C. Schmid, L. Klug, A.G. Sorgo, T. Eisenberg, S. Buttner, G.
929 Marino, R. Koziel, P. Jansen-Durr, K.U. Frohlich, G. Kroemer, and F. Madeo. 2014.
930 Lifespan extension by methionine restriction requires autophagy-dependent vacuolar
931 acidification. *PLoS Genet*. 10:e1004347.
932 Rutherford, A.C., C. Traer, T. Wassmer, K. Pattni, M.V. Bujny, J.G. Carlton, H. Stenmark,
933 and P.J. Cullen. 2006. The mammalian phosphatidylinositol 3-phosphate 5-kinase
934 (PIKfyve) regulates endosome-to-TGN retrograde transport. *J Cell Sci*. 119:3944-
935 3957.
936 Sbrissa, D., O.C. Ikonomov, and A. Shisheva. 1999. PIKfyve, a mammalian ortholog of yeast
937 Fab1p lipid kinase, synthesizes 5-phosphoinositides. Effect of insulin. *J Biol Chem*.
938 274:21589-21597.
939 Sbrissa, D., and A. Shisheva. 2005. Acquisition of unprecedented phosphatidylinositol 3,5-
940 bisphosphate rise in hyperosmotically stressed 3T3-L1 adipocytes, mediated by
941 ArPIKfyve-PIKfyve pathway. *J Biol Chem*. 280:7883-7889.
942 Sherman, F. 1991. [1] Getting started with yeast. Elsevier. 3-21.
943 Stauffer, W., H. Sheng, and H.N. Lim. 2018. EzColocalization: An ImageJ plugin for
944 visualizing and measuring colocalization in cells and organisms. *Sci Rep*. 8:15764.
945 Takatori, S., T. Tatematsu, J. Cheng, J. Matsumoto, T. Akano, and T. Fujimoto. 2016.
946 Phosphatidylinositol 3,5-Bisphosphate-Rich Membrane Domains in Endosomes and
947 Lysosomes. *Traffic*. 17:154-167.
948 Tsujita, K., T. Itoh, T. Ijuin, A. Yamamoto, A. Shisheva, J. Laporte, and T. Takenawa. 2004.
949 Myotubularin regulates the function of the late endosome through the gram domain-
950 phosphatidylinositol 3,5-bisphosphate interaction. *J Biol Chem*. 279:13817-13824.
951 Vines, J.H., H. Maib, C.M. Buckley, A. Gueho, Z. Zhu, T. Soldati, D.H. Murray, and J.S.
952 King. 2023. A PI(3,5)P2 reporter reveals PIKfyve activity and dynamics on
953 macropinosomes and phagosomes. *J Cell Biol*. 222.

954 Yorimitsu, T., and D.J. Klionsky. 2005. Atg11 links cargo to the vesicle-forming machinery
955 in the cytoplasm to vacuole targeting pathway. *Mol Biol Cell*. 16:1593-1605.
956

Figure 1

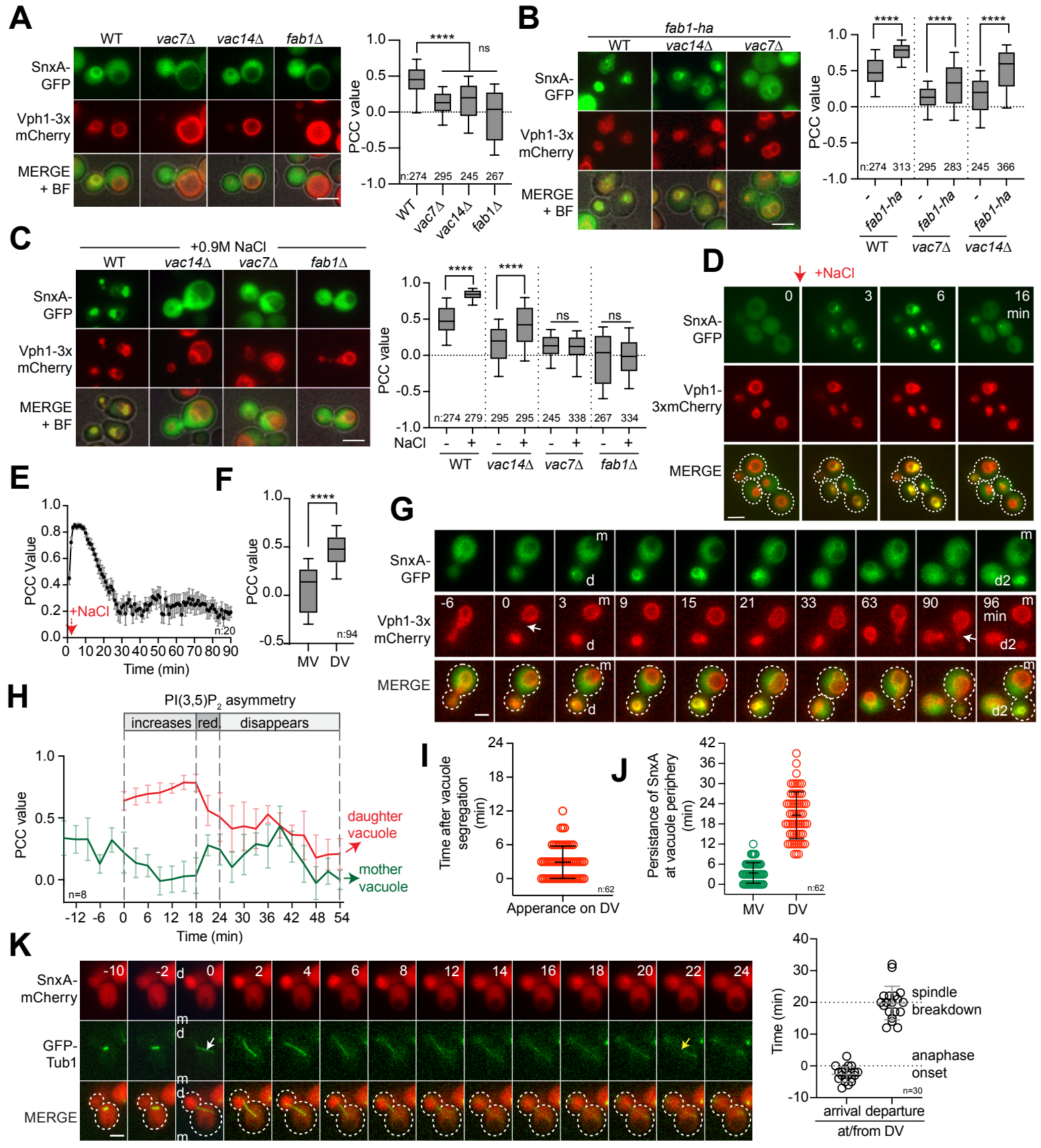
A
WT
vac7Δ
vac14Δ
fab1Δ
SnxA-GFP
Vph1-3x mCherry
MERGE + BF
PCC value
****
ns
n:274 295 245 267
B
fab1-ha
WT
vac14Δ
vac7Δ
n:274 313 295 283 245 366
C
+0.9M NaCl
NaCl
n:274 279 295 295 245 338 267 334
D
+NaCl
0
3
6
16 min
Vph1-3xmCherry
E
PCC Value
Time (min)
n:20
F
MV
DV
n:94
G
m
d
d2
-6
0
3
9
15
21
33
63
90
96 min
H
PI(3,5)P2 asymmetry
increases
red.
disappears
daughter vacuole
mother vacuole
n=8
I
Time after vacuole segregation (min)
Apperance on DV
n:62
J
Persistance of SnxA at vacuole periphery (min)
K
SnxA-mCherry
GFP-Tub1
spindle breakdown
anaphase onset
arrival departure
at/from DV
n=30

Figure 2

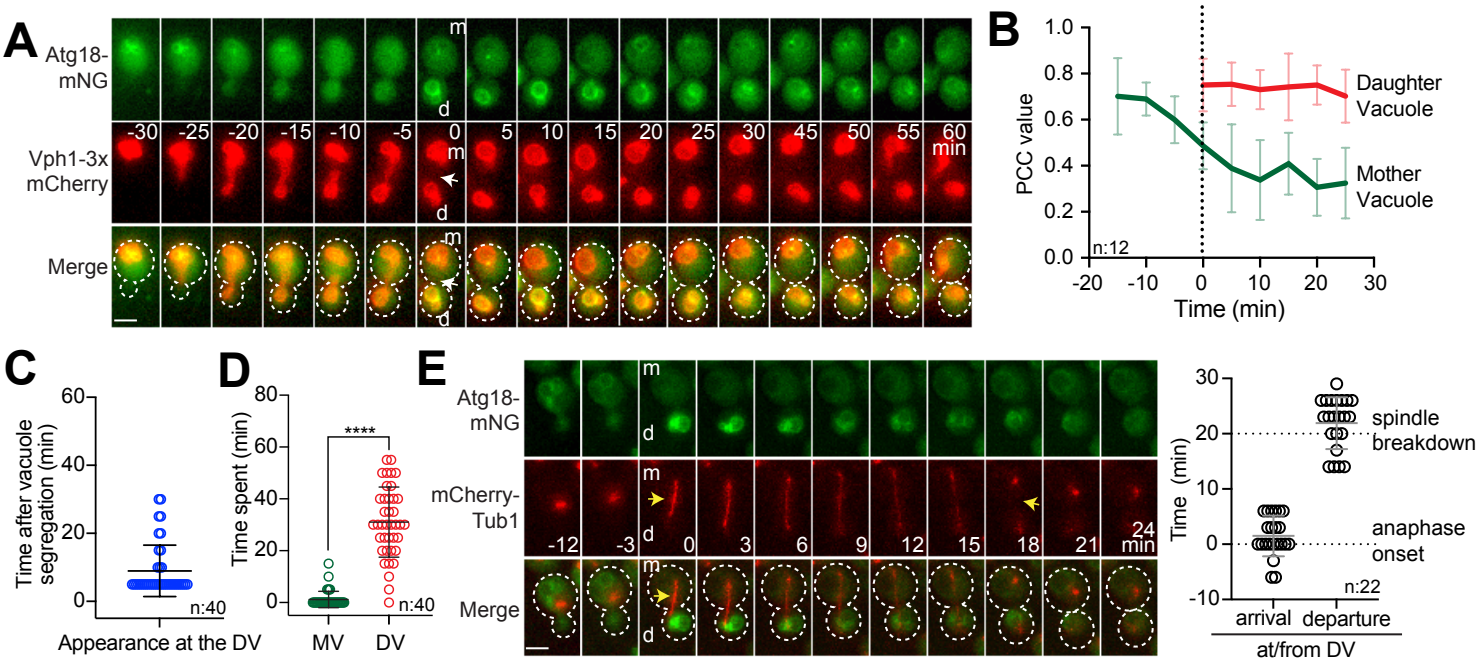
A
Atg18-mNG
Vph1-3x mCherry
Merge
-30 -25 -20 -15 -10 -5 0 5 10 15 20 25 30 45 50 55 60 min
m
d
B
PCC value
Time (min)
Daughter Vacuole
Mother Vacuole
n:12
C
Time after vacuole segregation (min)
Appearance at the DV
n:40
D
Time spent (min)
****
MV
DV
n:40
E
Atg18-mNG
mCherry-Tub1
Merge
-12 -3 0 3 6 9 12 15 18 21 24 min
Time (min)
spindle breakdown
anaphase onset
n:22
arrival
departure
at/from DV

Figure 3

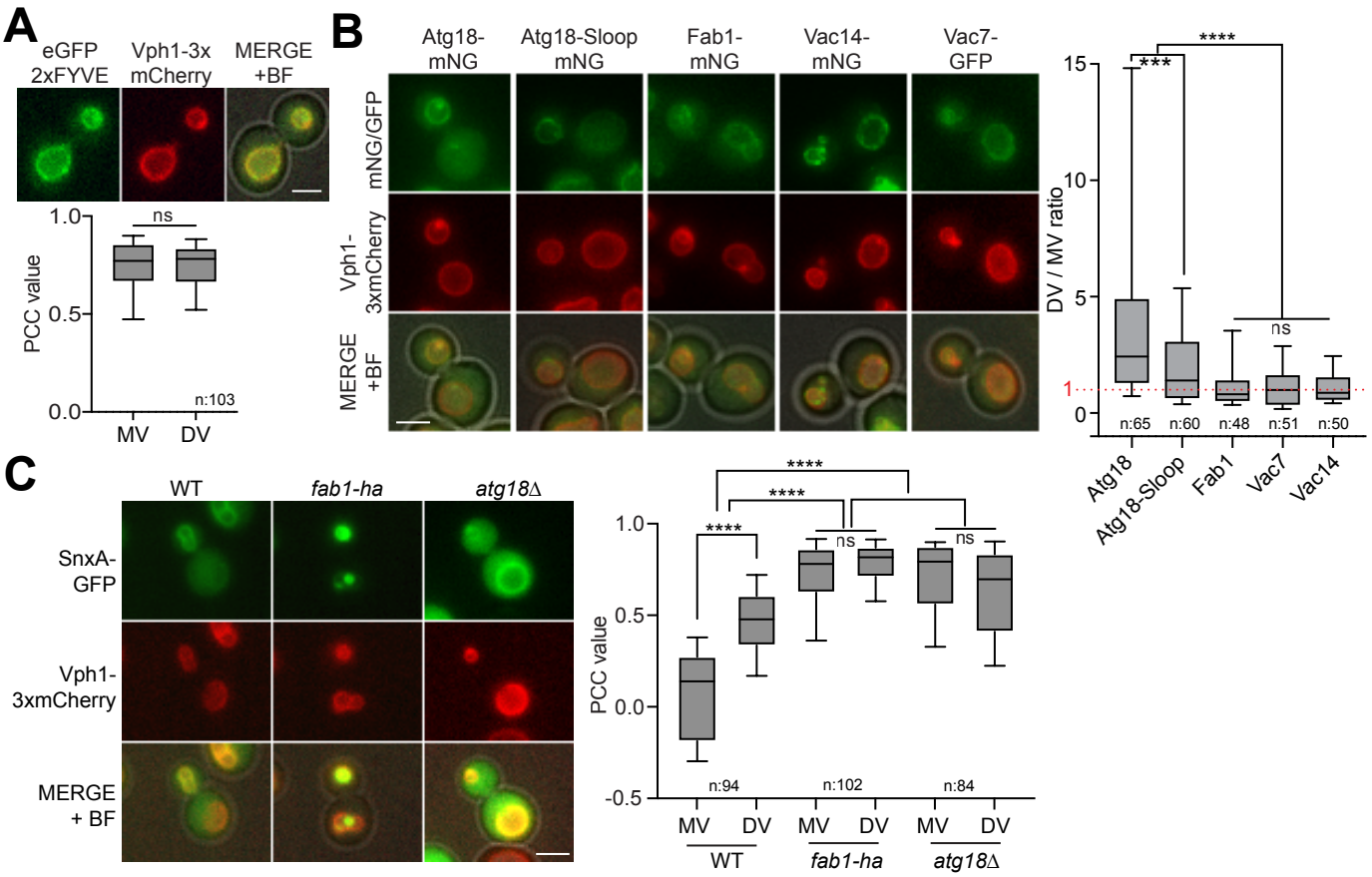
A
eGFP 2xFYVE
Vph1-3x mCherry
MERGE +BF
PCC value
1.0
0.5
0.0
ns
n:103
MV
DV
B
Atg18-mNG
Atg18-Sloop mNG
Fab1-mNG
Vac14-mNG
Vac7-GFP
mNG/GFP
Vph1-3xmCherry
MERGE +BF
DV / MV ratio
15
10
5
1
0
****
***
ns
n:65
n:60
n:48
n:51
n:50
Atg18
Atg18-Sloop
Fab1
Vac7
Vac14
C
WT
fab1-ha
atg18Δ
SnxA-GFP
Vph1-3xmCherry
MERGE + BF
PCC value
1.0
0.5
0.0
-0.5
****
****
****
ns
ns
n:94
n:102
n:84
MV
DV
MV
DV
MV
DV
WT
fab1-ha
atg18Δ

Figure 4

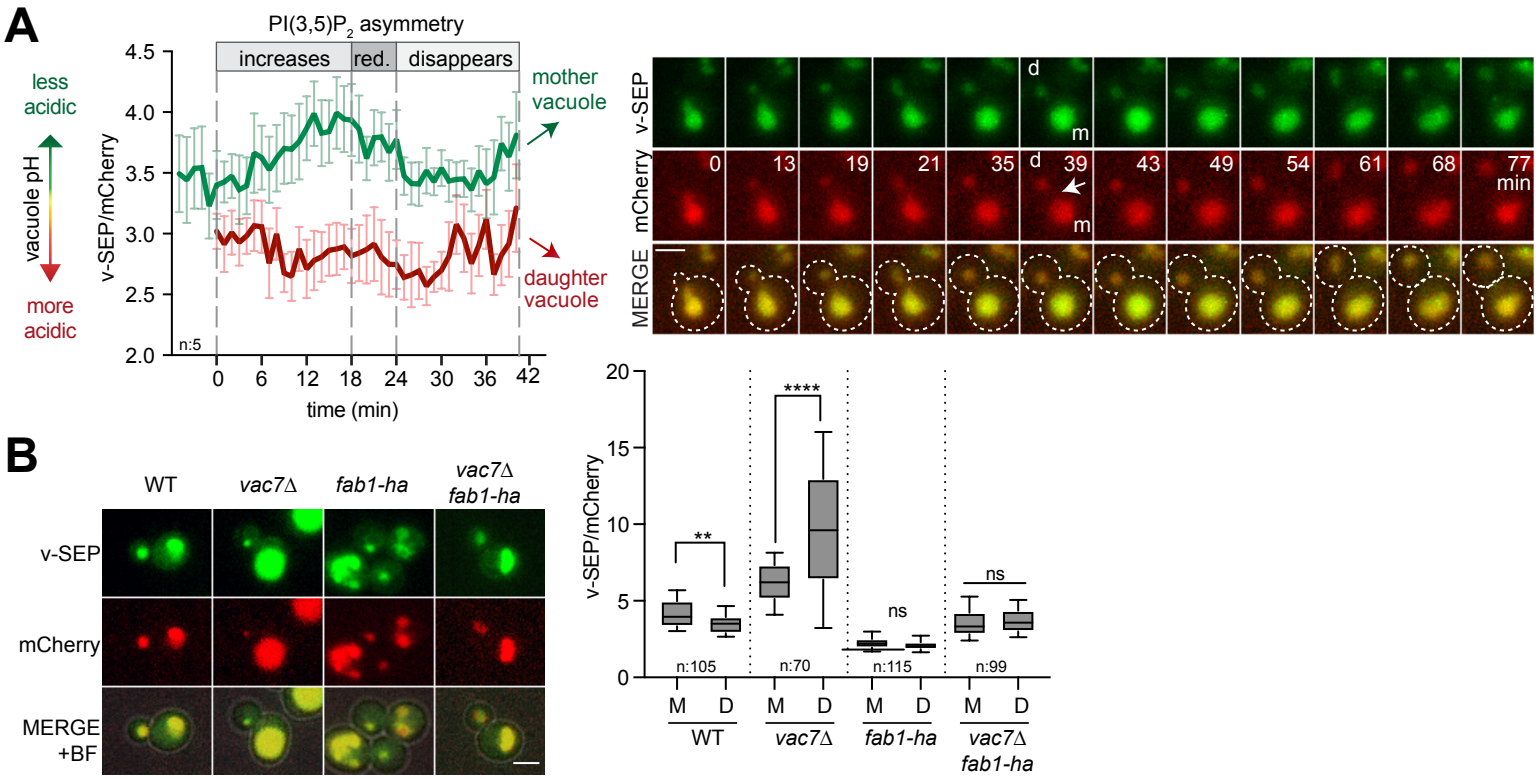
A
PI(3,5)P2 asymmetry
increases
red.
disappears
less acidic
vacuole pH
more acidic
v-SEP/mCherry
4.5
4.0
3.5
3.0
2.5
2.0
n:5
0
6
12
18
24
30
36
42
time (min)
mother vacuole
daughter vacuole
v-SEP
mCherry
MERGE
d
m
0
13
19
21
35
39
43
49
54
61
68
77
min
B
WT
vac7Δ
fab1-ha
vac7Δ fab1-ha
v-SEP
mCherry
MERGE +BF
v-SEP/mCherry
20
15
10
5
0
**
****
ns
ns
n:105
n:70
n:115
n:99
M
D
WT
vac7Δ
fab1-ha
vac7Δ fab1-ha

Figure 5

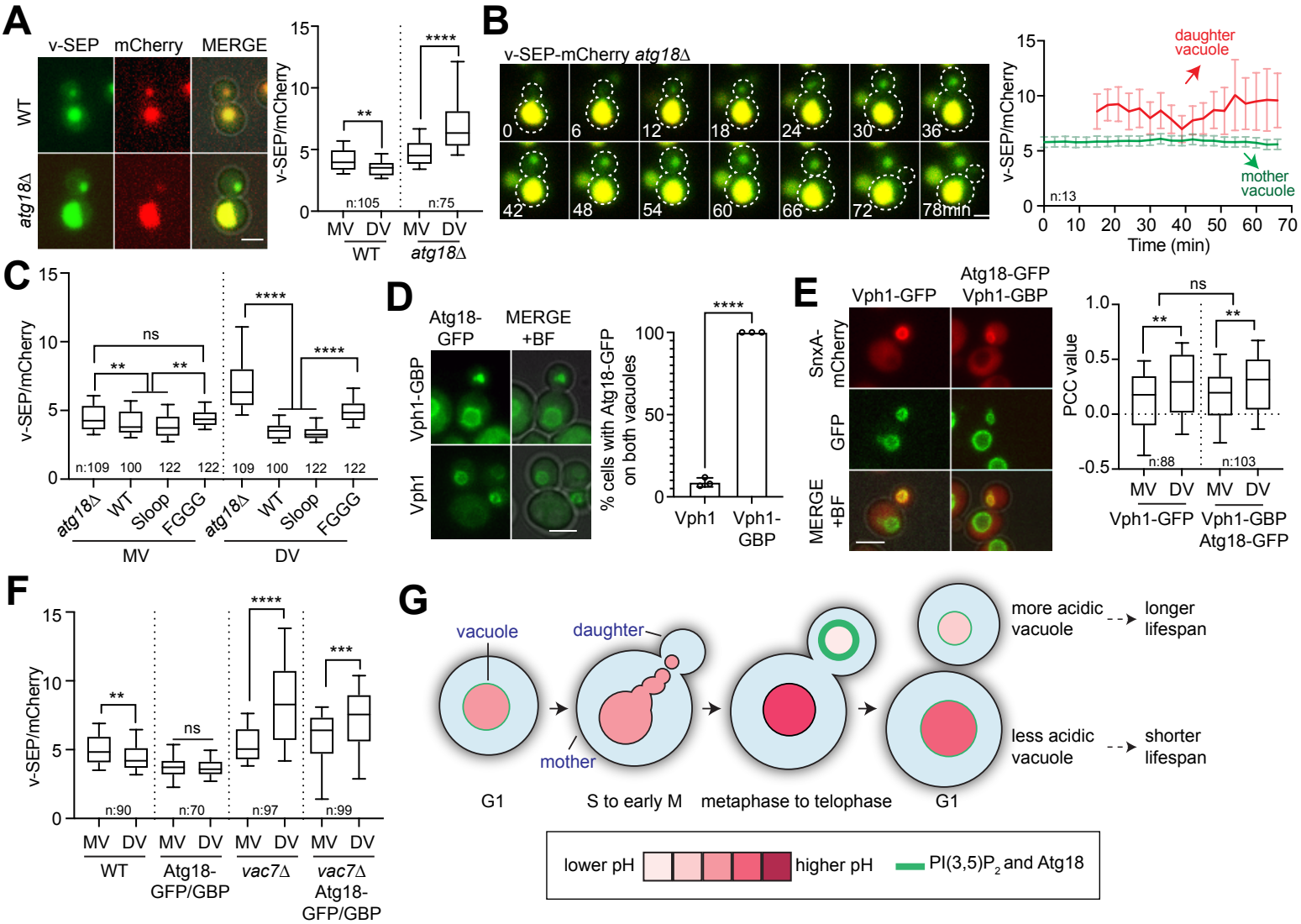
A
v-SEP
mCherry
MERGE
WT
atg18Δ
v-SEP/mCherry
**
****
n:105
n:75
MV DV MV DV
WT
atg18Δ
B
v-SEP-mCherry atg18Δ
0 6 12 18 24 30 36
42 48 54 60 66 72 78min
daughter vacuole
mother vacuole
n:13
Time (min)
C
ns
**
**
****
****
n:109 100 122 122 109 100 122 122
atg18Δ WT Sloop FGGG atg18Δ WT Sloop FGGG
MV
DV
D
Atg18-GFP
MERGE +BF
Vph1-GBP
Vph1
% cells with Atg18-GFP on both vacuoles
****
Vph1
Vph1-GBP
E
Vph1-GFP
Atg18-GFP Vph1-GBP
SnxA-mCherry
GFP
MERGE +BF
PCC value
ns
**
**
n:88
n:103
Vph1-GFP
Vph1-GBP Atg18-GFP
F
**
ns
****
***
n:90
n:70
n:97
n:99
WT
Atg18-GFP/GBP
vac7Δ
vac7Δ Atg18-GFP/GBP
G
vacuole
daughter
mother
G1
S to early M
metaphase to telophase
G1
more acidic vacuole
longer lifespan
less acidic vacuole
shorter lifespan
lower pH
higher pH
PI(3,5)P2 and Atg18